# Molecular dynamics study of ablation of solids under femtosecond laser pulses

Danny Perez and Laurent J. Lewis [a]

[a]Département de physique et Groupe de recherche en physique et technologie des couches minces (GCM), Université de Montréal, C. P. 6128 Succursale Centre-Ville, Montréal (Québec) H3C 3J7, Canada

We study the mechanisms of ablation of solids under femtosecond laser pulses using a two-dimensional molecular-dynamics model. By using a novel method to obtain the thermodynamic relaxation path of different sections of the target in the phase diagram, it is shown that four mechanisms can account for ablation for fluences (energy injected per unit surface) under the threshold for plasma formation: (i) spallation resulting from the loss of stability of the solid target following the passage of a tensile pressure wave; (ii) phase explosion resulting from important homogeneous nucleation of gas bubbles inside a superheated, metastable liquid; (iii) fragmentation of a highly strained supercritical fluid; and (iv) complete vaporization of the surface layers of the target. As many as three of these mechanisms can be active at the same time, inducing ablation of material at different depths under the surface of the sample. The occurrence of these mechanisms is linked to the characteristics of the thermodynamic relaxation path followed by the material after the absorption of the laser pulse.

*Nous étudions les mécanismes d'ablation des solides par des impulsions laser femtosecondes en utilisant un modèle de dynamique moléculaire bidimensionnel. En utilisant une nouvelle méthode d'obtention du chemin de relaxation thermodynamique de différentes sections de la cible dans le diagramme de phase, on montre que quatre mécanismes peuvent expliquer l'ablation pour des fluences (énergie injectée par unité de surface) sous le seuil de formation de plasma : (i) spallation résultant de l'instabilité de la cible solide après le passage d'une onde de pression tensile; (ii) explosion de phase résultant de la nucléation de bulles de gaz au sein d'un solide surchauffé; (iii) fragmentation d'un fluide surcritique fortement contraint; et (iv) évaporation complète de la couche de surface de la cible. Jusqu'à trois de ces mécanismes peuvent être actifs en même temps, causant une ablation à des profondeurs différentes sous la surface. L'existence d ces mécanismes est liée aux caractéristiques du chemin de relaxation thermodynamique suivi par le matériau après l'absorption de l'impulsion laser.*

## 1 Introduction

When a laser is shined on a solid target, material can be ejected following the intense heating caused by the light absorption. This process — laser ablation — plays an incresingly important role in many different technological applications. These include thin film growth, micromachining and chemical analysis, to name only a few. In the last decade, it was made clear that very short pulses (lasting pico or femtoseconds) can offer numerous advantages over longer ones (high yield and limited thermal damages to the target, for example).

To be efficient, these applications require a precise control of the properties of both the ablated material (yield, stoichiometry, size distribution and temperature of clusters) when used in thin-film growth or chemical analysis, and of the remaining sample (ablation depth, crater profile, extent of the thermal and mechanical damages) when used in a micro-machining setting. However, the basic mechanisms leading to ablation are still subject to debate, largely because theoretical modeling is difficult. Indeed, absorption of a large quantity of energy on such short timescale induces many different processes. On a microscopic scale, these include: dielectric breakdown in transparent solids, [1] change of optical and electronic properties, [2] nonthermal melting of covalent materials, [3] and semiconductor-to-metal transitions. [4] On a mesoscopic scale, the pressure wave generation, [5–7] the thermodynamical evolution of the expanding matter, [8,9] and the identification of the collective ejection processes [8,10–17] must all be understood in order to provide a complete picture of the phenomenon. Clearly, a complete microscopic description of the ablation process is out of reach of present models.

However, for fluences below the threshold for plasma formation, experiments show that ablation occurs hundreds of picoseconds after the absorption of the pulse [18]. This time is longer than the time required for the equilibrium between electronic and atomic degrees of freedom to establish. Hence, the details of the complex non-thermal processes which occur shortly after the absorption of the pulse are not expected to play a crucial role in the material removal. Ablation should thus be dominated by the thermodynamics or by processes occurring on a mesoscopic scale. Taking advantage of this simplifying factor, we identify the relevant ablation mechanisms for low fluences. We show that ablation involves four different processes — spallation, homogeneous nucleation, fragmentation and vaporization — which sometimes occur simultaneously at different positions under the surface of the target. A complete account of this study can be found in Refs. [17] and [19].

## 2 Computational Methods

### 2.1 Model

We study the ablation process using molecular dynamics in two dimensions. This type of simulations consists in integrating the equation of motion of the atoms in the system [20]. This integration is here carried out using the velocity-Verlet algorithm, which proceeds in two steps: first, updated positions and mid-step velocities are obtained from

$$x_i(t+\delta t) = x_i(t) + \delta t v_i(t) + \frac{1}{2}\delta t^2 a_i(t) \qquad (1)$$

and

$$v_i(t+\frac{1}{2}\delta t) = v_i(t) + \frac{1}{2}\delta t a_i(t). \quad (2)$$

At this point, the forces (and hence the accelerations) at time $t+\delta t$ are obtained using the updated positions. Finally, the velocities are adjusted using

$$v_i(t+\delta t) = v_i(t+\frac{1}{2}\delta t) + \frac{1}{2}\delta t a_i(t+\delta t). \quad (3)$$

The forces are deduced from an *a priori* specified interatomic potential, in our case a simple Lennard-Jones potential adjusted so as to vanish at the cutoff distance $r_c$:

$$\begin{aligned} \phi_{\mathrm{LJ}}(r) = \quad & 4\epsilon[(\sigma/r)^{12} - (\sigma/r)^6 \qquad r \le r_c \\ & -(\sigma/r_c)^{12} + (\sigma/r_c)^6] \\ \phi_{\mathrm{LJ}}(r) = \quad & 0 \qquad\qquad\qquad\qquad\quad r > r_c \end{aligned}$$

with $\epsilon$ (typically a few eV) and $\sigma$ (a few angströms) the usual energy and length scales, respectively. In the following, all results are reported in reduced units, i.e., $\epsilon/k_B$ for temperature and $\tau = (m\sigma^2/\epsilon)^{1/2}$ for time ($m$ is the atomic mass).

The usual optimization procedures were implemented in our code. First, to shorten the time required for the force calculation, a neighbor list is kept for every atom. However, since the state of the system changes strongly during a simulation, these lists have to be updated periodically. This is carried out using the cells and linked-list method [20]. With these optimizations, the computational load is proportional to the number of atoms in the system.

Simulation were carried out using samples consisting of 800 atomic layers in the $y$ direction and 500 layers in the $x$ direction, for a total of 400 000 atoms initially forming a triangular lattice thermalized at low temperature.

In order to simulate the ablation process, other components were added to the MD code; they are schematically presented in Fig. 1. We model the laser pulse (incident in the $y$ direction) as an ensemble of discrete photons of energy $4.5\epsilon$. The pulse has a Gaussian temporal profile with a width at half maximum of $\Delta t = 0.5\tau$ ($\sim 100$ fs) and a constant spatial profile. The depth at which the photons are absorbed in the target is chosen randomly so that the absorption profile follows a Beer-Lambert law ($I = I_0 e^{-\alpha y}$) where $\alpha = 0.002\sigma^{-1}$ is the absorption coefficient. During absorption, the photon energy is transfered to a "carrier". Here, a carrier is a particle which follows a Drude dynamics, i.e., the dynamics is governed by successive collisions occurring on average every $0.005\tau$. Evolution of the carrier gas proceeds in a Monte Carlo fashion. At each collision between a carrier and an atom, the former is allowed to emit a small quantity of energy ($0.07\epsilon$) that is converted into heat. This mimics the emission of phonons during the relaxation of the hot carrier gas.

The important pressure waves produced following the rapid heating of the surface region of the sample are absorbed using special boundary conditions at the bottom of the sample [21]. Periodic boundary conditions are used in the $x$ direction.

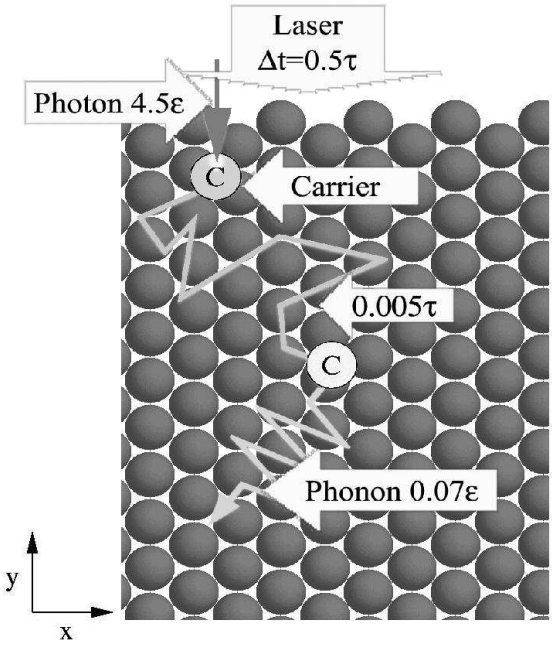


**Figure 1.** Schematic representation of the model system. See text for details.

With this model, a typical ablation simulation involves integrating the equation of motion over 120 000 time-steps ($600\tau \simeq 120$ ps). This take about 10 days on a single SGI R12000 CPU.

### 2.2 Calculation of local thermodynamic properties

The analysis which follows relies heavily on local, phase-specific thermodynamic properties of small subsections of the system. Specifically, we are interested in following the thermodynamic evolution of groups of atoms that have absorbed similar quantities of energy. We are also interested in the time evolution of the morphology of the material. Here we describe the method used to obtain this information.

First, the sample is separated into four-atomic-layer-thick "slices" perpendicular to the incident pulse. This grouping is preserved during the whole simulation. To minimize the effect of mixing between adjacent slices, only the $N$ atoms lying within one standard deviation of the mean $y$ position of atoms in the slice are used to compute the local thermodynamic quantities $\rho, T$ and $P$ as a function of time. The temperature and pressure are obtained using

$$T = \frac{1}{2N}\sum_{i=1}^{N}(v_i - v_{cm})^2 \quad (4)$$

and

$$P = A^{-1}(\mathcal{W} + NT), \quad (5)$$

where $v_{cm}$ is the center-of-mass velocity of the slice, $\mathcal{W}$ the virial sum and $A$ the area occupied by the slice. This

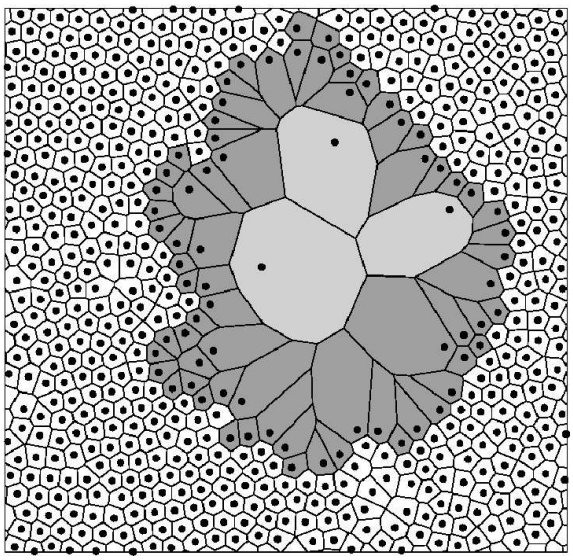

**Figure 2.** Phase-specific density calculation. White: condensed bulk atoms; dark gray: condensed surface atoms; light gray: isolated atoms.

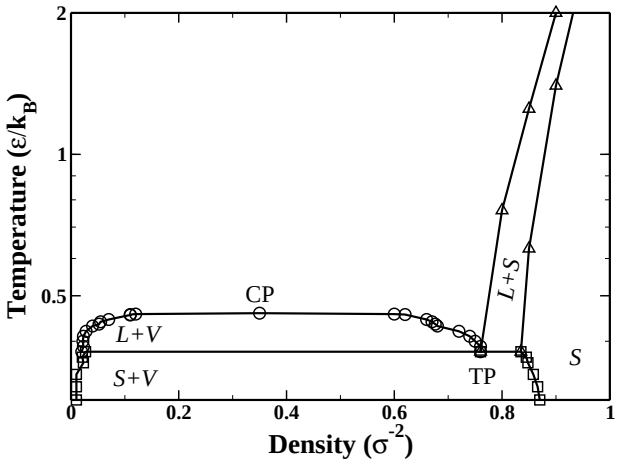


**Figure 3.** Phase diagram of the 2D truncated and shifted Lennard-Jones potential in the $\rho - T$ plane. Circles: binodal line (liquid-vapor coexistence); squares: solid-vapor coexistence line; triangles: solid-liquid coexistence line. The solid line is drawn to guide the eye. The italic letters refer the the phases in each regions (*S*,*L*,*V*: solid, liquid and vapor respectively). **CP**: critical point, **TP**: triple point.

last quantity (also required to obtain the density) is most difficult to obtain reliably. To circumvent this difficulty, we use a tessellation of space into Voronoi polygons centered around atomic positions. The area occupied by the slice is then taken as the sum of the area of the Voronoi polygons of atoms in this slice. This process is illustrated in Fig. 2. The thermodynamic trajectory obtained this way is refered to as *average*.

To couple thermodynamic and structural informations about a given slice, two other *phase-specific* trajectories were also defined: a *condensed* and a *gas* branch. In order to do this, clustered and isolated atoms are first identified using the Hoshen-Kopelman algorithm [22] with a clustering radius chosen so that the critical point density separates the gas and condensed phases. The condensed atoms are then separated into two subgroups: bulk (fully-coordinated) and surface (under-coordinated). The area occupied by the condensed phase is defined as the total number of condensed atoms times the mean area of the Voronoi atoms in the bulk subgroup (see Fig. 2). The difference between the total area of the slice and the area occupied by the condensed phase is attributed to the gas phase. The thermodynamic quantities are finally obtained using Eqs. 4 and 5 by averaging over the appropriate subgroup of atoms.

With this method, the onset of void formation is signaled by a split between the average and condensed branches. Further, the ratio of the densities on the different branches is an indication of the porosity and of the gas content of this part of the target.

### 2.3 Phase diagram

The method just described is not useful unless the phase diagram of the model system is known. For this purpose we used Monte Carlo simulations in the Gibbs ensemble [23] to complete a previously published section of the phase diagram [24]. The results are shown in Fig. 3. Properties of specific regions of this phase diagram will be discussed later on, as required by the discussion.

## 3 Results

### 3.1 Visual analysis

We first discuss the global reaction of the system after the absorption of the pulse in a qualitative manner by presenting snapshots of the simulation at different moments during the ablation process. The evolution of the system at low fluence ($F = 1.2F_{\rm th}$, where $F_{\rm th}$ is the threshold fluence for ablation) is exhibited in Fig. 4. Here, the laser pulse is fired during the first $2\tau$ of the simulation. In spite the important heating occurring during the relaxation of the carrier gas, the target does not react appreciably until $t = 5\tau$. At this point, a very important pressure wave generated by the isochoric heating is emitted and expansion of the target begins. Aside from the ejection of a few monomers, it can be seen that it takes about $100\tau$ for voids to form in the surface region. By $t = 200\tau$, it is apparent that the pores are filled with gas. These bubbles then continue to grow and coalesce until ablation is induced. In this case, two regions are easily distinguished: the non-ablated solid-region and the porous region, labeled I and II respectively.

Figure 5 shows that the situation becomes more complex as the fluence is increased to $F = 2.8F_{\rm th}$. Expansion and emission of monomers is now much more intense than at lower fluence. By $t = 100\tau$, a few voids begin to appear

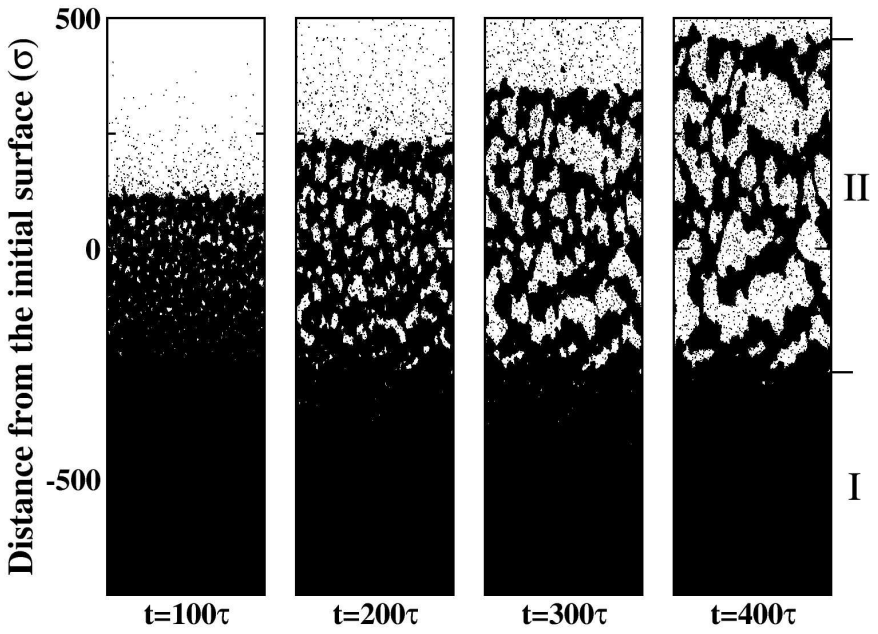


**Figure 4.** Snapshots of a simulation with $F = 900\epsilon/\sigma = 1.2\,F_{\rm th}$ and $\alpha = 0.002\sigma^{-1}$. Roman numerals identify different regions of the target (see text).

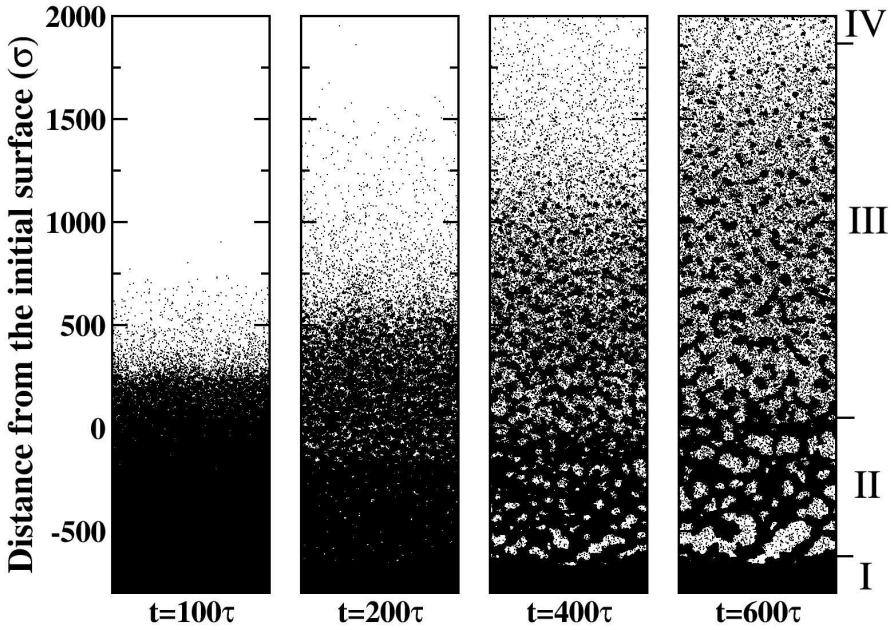


**Figure 5.** Snapshots of a simulation with $F = 2100\epsilon/\sigma = 2.8\,F_{\rm th}$ and $\alpha = 0.002\sigma^{-1}$. Roman numerals identify different regions of the target. Region IV is the gaseous region (out of the range of the last snapshot).

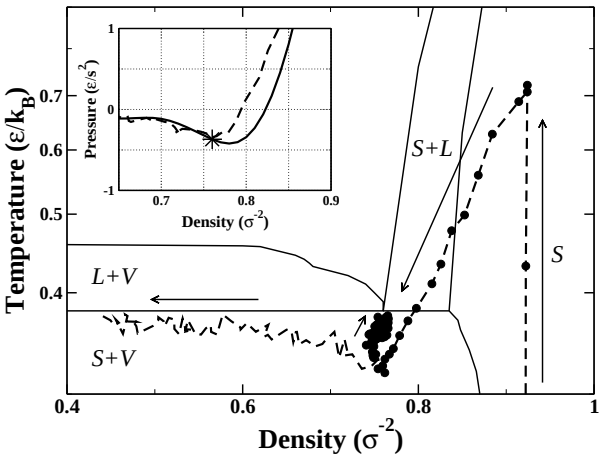


**Figure 6.** Typical thermodynamic evolution for regions of the target where spallation occurs. Dashed line: average branch; filled circles: condensed branch. Arrows indicate the flow of time. Inset: average trajectory in the $\rho - P$ plane (dashed line) and $T = 0.36$ isotherm (solid line). The star indicates the point of fracture.

close to the surface. In the following $300\tau$, the surface region is totally decomposed into small liquid clusters. Evaporation from the surface of these hot clusters quickly fill the surroundings with gas. At $t = 400\tau$, gas-filled pores begin to form deeper into the target. The morphology of this region quickly becomes very similar to that of region II in Fig. 4. In this case, four different regions can thus be identified inside the sample: a non-ablated solid region I, a porous region II, a cluster-filled region III and a purely gaseous region IV. The strongly-varying morphologies of these regions suggests that different ablation mechanisms may be effective as a function of depth, and hence as a function of locally absorbed energy. (Recall that the energy locally absorbed decreases exponentially with depth). By following the thermodynamic evolution of the material in every one of these regions, it will now be shown that this is indeed the case.

## 3.2 Mechanisms of ablation

### *3.2.1 Spallation*

While not apparent in Figs. 4 and 5, ablation can occur from the solid phase (region I) in specific conditions, namely when strong tensile pressure waves are running through the system. If ablation occurs following mechanical fracture caused by the passage of such wave, one speaks of spallation. This mechanism was already observed in experiments of ablation on gels [14] and biological tissues [7]. Simulations of ablation of organic solids in the stress-confinement regime have also been interpreted in terms of a spallation-like process [15]. We now show that it could also be important in more cohesive solids.

Indeed, Fig. 6 shows a typical thermodynamic trajectory for a region of the target in which spallation occurs. First, it can be seen that the laser pulse initially heats the lattice up to a very high, supercritical, temperature; notice that the heating occurs at constant density for such short pulses. Expansion then quickly sets in and the temperature decreases below the triple point. At this moment, the system enters the solid-vapor coexistence region. Upon entrance in this region, a tensile wave (negative pressure wave) reaches this part of the sample (see inset of Fig. 6) and further stretches the material. The split between the average and condensed branches indicates that failure occurred during the passage of this wave, around $\rho \simeq 0.76\sigma^{-2}$. The average density then continues to decrease (the voids are growing) until ablation finally occurs. The inset shows that fracture occurred because the system was pushed into a mechanically unstable state by the passage of the pressure wave. Indeed, mechanical stability requires a positive isothermal compressibility, i.e., a positive slope of the isotherm in the $\rho - P$ plane of the phase diagram. It can be seen that this condition was violated just before signs of fracture were observed in this slice. Spallation is thus indeed responsible for ablation in this case.

### *3.2.2 Homogeneous nucleation*

When the energy injected in the system increases, relaxation eventually proceeds above the triple point, i.e., the system melts during its expansion. If the maximum temperature is not too high, the thermodynamic evolution of the material can bring the system into the liquid-vapor coexistence region. This corresponds to region II in Figs. 4 and 5.

In this region, the free-energy of the gas phase becomes lower than that in the liquid phase, i.e., the homogeneous liquid is no longer the most stable configuration. For long enough waiting times or a high enough degree of metastability, gas bubbles are expected to form inside the metastable liquid by a process called *homogeneous nucleation*. For high nucleation rates, the liquid can rapidly decompose into an equilibrium mixture of liquid droplets and monomers; in this case one speaks of *phase explosion*. This process is widely considered to be a common ablation process in the ultrashort pulse regime [8,10–12,25–27]. However, a clear evidence of its occurrence still lacks.

We now show that our simulations provide a direct confirmation of the relevance of homogeneous nucleation to the description of ablation. Fig. 7 presents the evolution of the system when the liquid-vapor coexistence region is entered. This figure shows that the onset of bubble nucleation (marked by the split between the average and condensed branches) occurred shortly *after* the entrance in the liquid-vapor metastable region. Further, the trajectories show clear signs of phase separation: i) the density of the liquid phase stays constant during the entire process and ii) the gas phase also stays at constant density, precisely on the liquid-vapor equilibrium line. Our simulations thus provide clear evidence that homogeneous nucleation is indeed responsible for ablation at moderate energy.

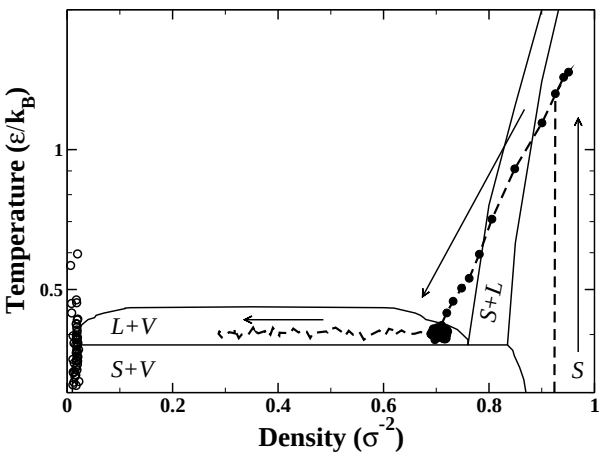


**Figure 7.** Typical thermodynamic evolution for regions of the target where homogeneous nucleation occurs. Dashed line: average branch; filled circles: condensed branch; empty circles: gas branch.

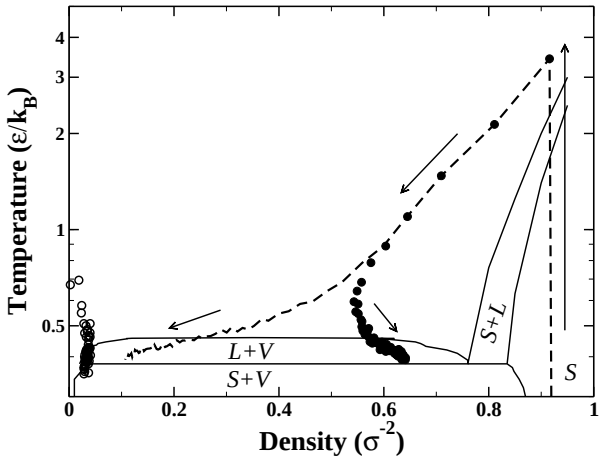


**Figure 8.** Typical thermodynamic evolution for regions of the target where fragmentation occurs. See Fig. 7 for the definition of symbols and lines.

### *3.2.3 Fragmentation*

As the energy continues to increase, relaxation at some point becomes supercritical, i.e., proceeds above the critical point. In this situation, homogeneous nucleation is no longer possible. This is the case for the material found in region III in Fig. 5.

A typical thermodynamic trajectory in this regime is shown in Fig. 8. The figure confirms that the void formation leading to ablation occurred *outside* of the liquid-vapor metastable region, so that homogeneous nucleation cannot be held responsible for ablation. Indeed, the split between the average and condensed branches occurs at a temperature exceeding the critical temperature. However, by comparing the different snapshots of Fig. 5, we see that expansion in region III proceeds at a very high rates compared to that in region II. This is a hint that ablation might have a mechanical origin in this case. Indeed, separation of supercritical fluids subject to important strain rates into small clusters has been observed before in numerous situations: computer simulation of two and three-dimensional Lennard-Jones systems under homogeneous expansion [28] and of rapid heating of liquid drops [29,30], experiments on the free-jet expansion of liquids [31,32], etc. This process is called fragmentation.

In this context, the size of the clusters formed during the expansion should decrease with increasing strain rate. This is verified in Fig. 9 where the mean cluster mass is plotted against the local strain rate at their formation depth. Further, the apparent power-law dependence between these two quantities can be explained by a simple model due to Ashurst and Holian [28]. This model states that fragmentation results from the conversion of some of the internal stress stored in the expanding target into surface energy of clusters. For uniaxial expansion in two dimensions, this model predicts that the mean cluster mass should be given by:

$$M = 4\zeta\rho(r_0\gamma)^{2/3}\eta^{-4/3} \tag{6}$$

where $\zeta$ is a geometric factor of the order of unity, $\eta$ is the strain rate, $r_0$ is the equilibrium bond length, and $\gamma$ is the surface energy per unit mass. The same power-law dependence is predicted by the energy-minimization model of Grady [33,28] and thus constitutes a strong signature of fragmentation.

The prediction of the model is also plotted in Fig. 9 for comparison. One can see that the strain rate dependence is very well accounted for using this simple model. This thus confirms that fragmentation is responsible for ablation at high energy.

### *3.2.4 Vaporization*

Finally, if the energy injected by the laser is high enough, the surface layers of the target are completely atomized (cf. part IV of Fig. 5). Figure 10 shows the evolution of the material in this region. We see that the condensed and average branches split at a very early time and that the average and gas branches merge soon after inside the vapor region of the phase diagram, showing that the slice as a whole is behaving like a gas. The trajectory thus simply illustrates a vaporization process occuring when the energy injected by the laser pulse is comparable to the cohesive energy of the material.

## 4 Conclusion

By using molecular-dynamics simulation on a two-dimensional Lennard-Jones system we showed that low-fluence laser ablation in the ultrashort-pulse regime involves four different mechanisms: spallation, homogeneous nucleation, fragmentation and vaporization. The dif-

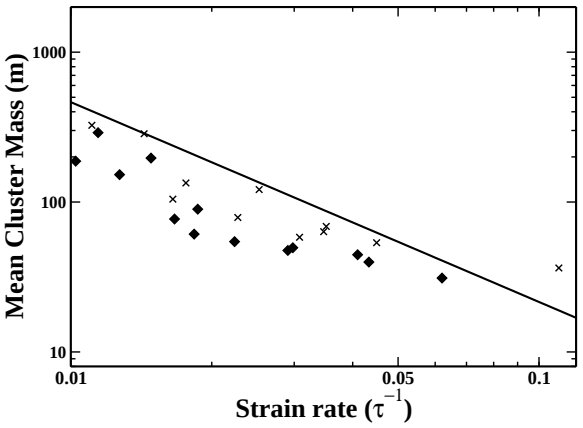


**Figure 9.** Mean cluster mass versus local strain rate for for $\alpha = 0.01\sigma^{-1}$. Crosses: $F = 750\epsilon/\sigma$; diamonds: $F = 900\epsilon/\sigma$. The solid line is Eq. 6.

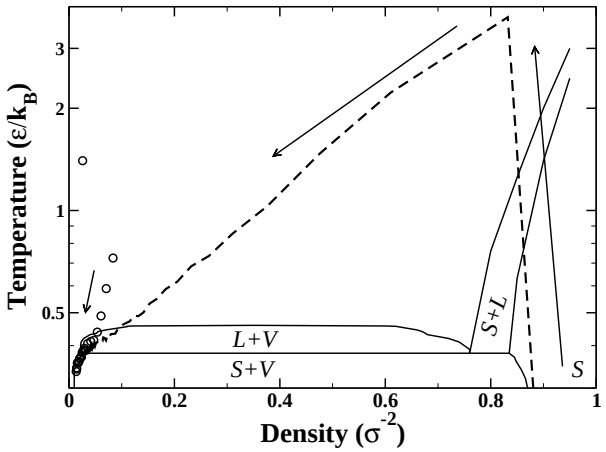


**Figure 10.** Typical thermodynamic evolution for regions of the target where vaporization occurs. See Fig. 7 for the definition of symbols and lines.

ferent mechanisms are effective in different ranges of energy, and hence can occur simultaneously at different positions inside the target. One of these mechanisms — fragmentation — is proposed for the first time in the context of laser ablation.

## Acknowledgments

We thank Patrick Lorazo, Ralf Meyer and Michel Meunier for numerous enlightening discussions. This work has been supported by grants from the Canadian *Natural Sciences and Engineering Research Council* (NSERC) and Québec's *Fonds québécois de la recherche sur la nature et les technologies* (FQRNT). We are indebted to the *Réseau québécois de calcul de haute performance* (RQCHP) for generous allocations of computer resources.

## References

1. A. Kaiser, B. Rethfeld, M. Vicanek, and G. Simon. Microscopic processes in dielectrics under irradiation by subpicosecond laser pulses. *Physical Review B*, 61:11 437, 2000.
2. J.S. Graves and R.E. Allen. Response of gaas to fast intense laser pulses. *Physical Review B*, 58:13 627, 1998.
3. K. Sokolowski-Tinten, J. Bialkowski, M. Boing, A. Cavalleri, and D. von der Linde. Thermal and nonthermal melting of gallium arsenide after femtosecond laser excitation. *Physical Review B*, 58:11 805, 1998.
4. J.P. Callan, A.M.-T. Kim, C.A.D. Roeser, and E. Mazur. Universal dynamics during and after ultrafast laser-induced semiconductor-to-metal transitions. *Physical Review B*, 64:073201, 2001.
5. J. C. Bushnell and D. J. McCloskey. Thermoelastic stress production in solids. *J. Appl. Phys.*, 39:5541, 1968.
6. J. I. Etcheverry and M. Mesaros. Molecular dynamics simulation of the production of acoustic waves by pulsed laser irradiation. *Physical Review B*, 60:9430, 1999.
7. I. Itzkan, D. Albagli, M.L. Dark, L.T. Perelman, C. von Rosenberg, and M.S. Fields. The thermoelastic basis of short pulsed laser ablation of biological tissues. *Proc. Natl. Acad. Sci. USA*, 92:1960, 1995.
8. K. Sokolowski-Tinten, J. Bialkowski, A. Cavalleri, D. von der Linde, A. Oparin, J. Meyer ter Vehn, and S.I. Anisimov. Transient states of matter during short pulse laser ablation. *Phys. Rev. Lett.*, 81:224, 1998.
9. V.V. Zhakhovskii, K. Nishiara, S.I. Anisimov, and N.A. Inogamov. Molecular-dynamics simulations of rarefaction waves in media that can undergo phase transitions. *JETP Letters*, 71:167, 2000.
10. R. Kelly and A. Miotello. Comments on explosive mechanisms of laser sputtering. *Applied Surface Science*, 96-98:205–215, 1996.
11. A. Miotello and R. Kelly. Critical assessment of thermal models for laser sputtering at high fluences. *Applied Physics Letters*, 67:3535, 1995.
12. A. Miotello and R. Kelly. Laser-indiced phase explosion: new physical problems when a condensed phase approaches the thermodynamic critical temperature. *Applied Physics A*, 69:S69–S73, 1999.
13. B. N. Chichkov, C. Momma, S. Nolte, F. von Alvensleben, and A. Tünnermann. Femtosecond, picosecond and nanosecond laser ablation of solids. *Appl. Phys. A*, 63:109, 1996.
14. G. Paltaud and H. Schmidt-Kloiber. Microcavity dynamics during laser-induced spallation of liquids and gels. *Applied Physics A*, 62:303, 1996.
15. L. V. Zhigilei and B. J. Garrison. Microscopic mechanisms of laser ablation of organic solids in the thermal and stress confinement irradiation regimes. *J. Appl. Phys*, 88:1281, 2000.
16. F. Vidal, T.W. Johnston, S. Laville, O. Barthélemy, M. Chaker, B. Le Drogoff, J. Margot, and M. Sabsabi. Critical-point phase separation in laser ablation of conductors. *Phys. Rev. Lett.*, 86:2573, 2001.
17. D. Perez and L. J. Lewis. Ablation of solids under femtosecond laser pulses. *Physical Review Letters*, 89:255504, 2002.
18. D. von der Linde, K. Sokolowski-Tinten, and J. Bialkowski.

Laser-solid interaction in the femtosecond time regime. *Applied Surface Science*, 109:1, 1997.

19. D. Perez and L. J. Lewis. Molecular-dynamics study of ablation of solids under femtosecond laser pulses. *Physical Review B, in press*, 2003.
20. M.P. Allen and D.J. Tildesley. *Computer Simulation of Liquids*. Oxford Science Publications, Oxford, 1987.
21. L. V. Zhigilei and B. J. Garrison. Pressure waves in microscopic simulations of laser ablation. *Mat. Res. Soc. Symp. Proc.*, 538:491, 1999.
22. J. Hoshen and R. Kopelman. Percolation and cluster distribution. i. cluster multiple labelling technique and critical concentration algorithm. *Physical Review B*, 14:3438, 1976.
23. A. Z. Panagiotopoulos. Direct determination of phase coexistence properties of fluids by monte carlo simulation in a new ensemble. *Molecular Physics*, 61:813, 1998.
24. B. Smit and D. Frenkel. Vapor-liquid equilibria of the two-dimensional lennard-jones fluid(s). *J. Chem. Phys.*, 94:5663, 1991.
25. J.H. Yoo, S.H. Jeong, X.L. Mao, R. Grief, and R.E. Russo. Evidence for phase-explosion and generation of large particles during high power nanosecond laser ablation of silicon. *Applied Physics Letters*, 76:783, 1999.
26. J.H. Yoo, S.H. Jeong, R. Grief, and R.E. Russo. Explosive change in crater properties during high power nanosecond laser ablation of silicon. *Journal of Applied Physics*, 88:1638, 2000.
27. N.M. Bulgakova and A.V. Bulgakov. Pulsed laser ablation of solids: transition from normal vaporization to phase explosion. *Applied Physics A*, 73:199, 2000.
28. Wm. T. Ashurst and B. L. Holian. Droplet formation by rapid expansion of a liquid. *Phys. Rev. E*, 59:6742, 1999.
29. J. A. Blink and W. G. Hoover. Fragmentation of suddenly heated liquids. *Phys. Rev. A*, 32:1027, 1985.
30. A. Strachan and C. O. Dorso. Caloric curve in fragmentation. *Phys. Rev. C.*, 58:R632, 1998.
31. E. L. Knuth and U. Henne. Average size and size distribution of large droplets produced in a free-jet expansion of a liquid. *Journal of Chemical Physics*, 110:2664–2668, 1999.
32. Wm. T. Ashurst and B. L. Holian. Droplet size dependance upon volume expansion rate. *Journal of Chemical Physics*, 111:2842–2843, 1999.
33. D. E. Grady. Local inertial effects in dynamic fragmentation. *J. Appl. Phys.*, 51:322, 1981.